RSC Advances

ROYAL SOCIETY OF CHEMISTRY

www.rsc.org/advances

Core-shell TiO_2@C nano-architecture: facile synthesis, enhanced visible photocatalytic performance and electrochemical capacitance

Linrui Hou, [a] Hui Hua,[a] Hui Cao,[a] Siqi Zhu,[a] and Changzhou Yuan* [a, b]*

[a] *School of Materials Science and Engineering, Anhui University of Technology, Ma'anshan, 243002, P. R. China*

*Email:*houlr629@163.com (L.R. Hou); ayuancz@163.com (C. Z. Yuan)

[b] *Chinese Academy of Science (CAS) Key Laboratory of Materials for Energy Conversion, Hefei, 230026, P.R. China*

Abstract

In the work, we elegantly devised a bottom-up solvothermal strategy coupled with subsequent controllable calcination to synthesize core-shell TiO_2@C nanohybrid with a uniform ultrathin carbon shell of ~1 – 3 nm. Physicochemical investigations revealed that Rutin and ethylene glycol played a great role in successful *in-situ* fabrication of uniform core-shell nano-architecture. Benefiting from appealing synergetic effect of mesoporous core-shell structure and composition advantages, the resulting core-shell TiO_2@C with remarkable visible light response exhibited enhanced photocatalytic degradation efficiency and stability of methylene blue under visible light irradiation. Furthermore, the unique core-shell TiO_2@C, thanks to its large surface area, rich mesoporosity and high electronic conductivity, demonstrated excellent electrochemical capacitance with large specific capacitance of 210 F g^{-1} at 0.2 A g^{-1}, and ~2% capacitance degradation over cycling for 1200 times in 0.5 M aqueous H_2SO_4 at a current rate of 1 A g^{-1}.

Keywords: TiO_2@C; Core-shell nano-architecture; Visible light photocatalysts; Electrochemical capacitors

1. Introduction

In last decades, nano-structured anatase titanium dioxide (TiO_2) has attracted considerable attention as a low-cost, nontoxic, green and environmentally-benign functional semiconductor,[1] and been studied and applied widely in versatile fields, including supports of fuel cell catalysts,[1] Li-ion batteries,[2] Li-S batteries,[3, 4] photoelectrochemical solar cells,[5] and so on. In particular, the utilization of various carbonaceous materials as the building block towards anatase TiO_2-based nanohybrids has been retrieved extensively for potential photocatalytic degradation of a variety of organic environmental pollutants,[6-9] and low-cost electroactive materials for electrochemical capacitors (ECs) [10-14] recently, in view of the striking synergetic effects of the carbon and TiO_2 phase.

As is well known, the catalytic efficiency of photocatalytic procedures strongly depends both upon the solar energy utilization and photo-generated electron/hole recombination rate.[6-9] As regards to the photocatalytic application, anatase TiO_2 is still limited seriously by its large band-gap energy (E_g, 3.2 eV) resulting in low utilization (just small ultraviolet fraction, < 4%) of the total solar spectrum if it is utilized alone.[15] Numerous efforts thus have been devoted to hybridize TiO_2 with carbonaceous materials by forming core-shell TiO_2@C architecture to extend the photo-response to the visible region. In this regards, elegant combination of the intrinsic photocatalytic activity of TiO_2 and the adsorptivity of carbonaceous materials is simultaneously obtained with the final aim to reduce electron-hole recombination rate, increase the light utilization efficiency, enhance the stability of the anatase phase and achieve a narrow band gap meanwhile.[7-9, 16, 17] Additionally, the non-polar, non-reactive and non-toxic nature of the carbon shell and easy separation of hybrid TiO_2@C with core-shell structure from aqueous solution are attractive greatly from a

commercial application of point of view.[17] However, the huge challenges by far inherent in the core-shell approach mainly lie in how to achieve a uniform and ultrathin carbon shell for a compromise between the photo-activity and photo-adsorption.[18] Moreover, the synthetic strategies of core-shell TiO_2@C generally involve in an extra-coating process,[1, 9, 11, 16] which makes the synthesis more sophisticate and increases the fabrication cost meanwhile. Therefore, it is of great significance yet urgent to explore simple but efficient strategy to realize the state-of-the-art design of uniform core-shell TiO_2@C nanohybrid with a ultrathin coating shell.

Furthermore, recent years have witnessed the application of TiO_2 for high-performance ECs as an intriguing electrode.[10-14] Unfortunately, owing to the intrinsically modest electrical conductivity (~10^{-5} – 10^{-2} S cm^{-1}) of the TiO_2 itself,[12, 19] low specific capacitances (SCs) of < 100 F g^{-1} are commonly observed.[10, 13] Charmingly, recent reports explicitly reveal that the carrier densities of nanophase TiO_2 can be enhanced significantly by 3 orders of magnitudes through the introduction of Ti^{3+} sites (*i.e.*, oxygen vacancy) upon hydrogenation at high temperatures.[12, 13] However, one should note that the utilization of hydrogen at enhanced temperatures are too dangerous to favor for the practical industrial application. Inspired by this, we hypothesize that it would be a better choice by constructing typical core-shell TiO_2@C nanohybrid, where the carbon shell with excellent electric double-layer capacitance (EDLC) would not only enhance electronic conductivity of the pristine TiO_2 by intimate adhesion to the conducting carbon, but also introduce Ti^{3+} ions *via* the carbonthermal reduction over high-temperature carbonization meanwhile. As a result, appealing electrochemical capacitance would be highly anticipated. Also of note, the newly-formed Ti^{3+} sites would boost the

visible light response of TiO_2 meantime,[8] promoting the visible catalytic performance of TiO_2-based photocatalysts.

Bearing these comprehensive considerations in mind, in the study, we purposefully designed and explored an efficient bottom-up solvothermal strategy coupled with following calcination to *in-situ* fabricate core-shell TiO_2@C nanohybrid with a uniform ultrathin carbon shell. The tentative underlying formation mechanism of uniform core-shell nano-architecture was also proposed herein. Thanks to the intriguing mesoporous core-shell feature and composition advantages, the resulting core-shell TiO_2@C nanohybrid presented remarkable photocatalytic degradation efficiency and stability of methylene blue (MB) under visible light irradiation, and attractive electrochemical capacitance in aqueous H_2SO_4 electrolyte when evaluated as a promising electrode for advanced ECs.

2. Experimental

Materials Synthesis All the aqueous solutions were prepared with Milli-Q water from a Milli-Q Plus system (Millipore). In a typical synthesis, 1.2 mmol of Rutin trihydrate ($C_{27}H_{30}O_{16}\cdot 3H_2O$, Sigma-Aldrich, > 99%) was dissolved in 120 mL of ethylene glycol (EG, Sigma-Aldrich, > 99.5%), which was denoted as the solution A. 0.2 mmol of $Ti(OBu)_4$ (TBOT) was added into 20 mL of EG under stirring vigorously at ambient temperature, which was designed as the solution B. The solution B was added dropwise into the solution A. Then, a mixed solution was obtained, and transferred to a Teflon-lined stainless steel autoclave for solvothermal reaction at 180 °C for 10 h in an electric oven. After cooled, the final product (denoted as Rutin-Ti) was collected by centrifugation, and washed with water and absolute ethanol in order, and further calcinated at 700 °C for 3 h in N_2 atmosphere with a ramp rate of 5 °C min^{-1}. After this, the sample was further annealed at 440 °C for 5

min in air with a heating rate of 5 °C min^{-1}. Accordingly, a black product (designed as TiO_2@C) was obtained. For comparison, white TiO_2 sample was fabricated by directly annealing the Rutin-Ti at 700 °C for 3 h in air with a ramp rate of 5 °C min^{-1}.

Materials Characterizations The samples were examined by powder X-ray diffraction (XRD) (Max 18 XCE, Japan) using a Cu K*a* source (λ = 0.154056 nm) at a scanning speed of 3° min^{-1} over a 2θ range of 10 ° – 80 °. The morphologies and structures were observed by using field-emission scanning electron microscopy (FESEM, JEOL-6300F, 15 kV), transmission electron microscope (TEM) with energy dispersive X-ray (EDX) analyzer, high-resolution transmission electron microscopy (HRTEM) and selected area electron diffraction (SAED) (JEOL JEM 2100 system operating at 200 kV). Fourier transform infrared (FT-IR) spectra were obtained on 360 Nicolet AVATAR. X-ray photoelectron spectra (XPS) measurement was performed on a VGESCALAB MKII X-ray photoelectron spectrometer with Mg k*a* excitation source (1253.6 eV). N_2 adsorption/desorption isotherms were determined by using an ASAP-2010 surface area analyzer. The Raman analysis of the sample was recorded by Laser Raman (T6400, Jobion yzon corp. France). Thermogravimetric (TG) analysis was carried out by using a TA instruments Q 500 analyzer under air flow with a temperature ramp of 10 °C min^{-1}.

Photocatalytic experiments Photocatalytic activities were investigated in aqueous solution in a water-cooled quartz cylindrical cell. The reaction mixture in the catalytic cell was maintained at 20 °C by a continuous flow of water and magnetic stirring, and illustrated with an internal xenon lamp (XHA 150 W) equipped with a cut-off glass filter transmitting λ > 400 nm. A MB solution was prepared with an initial concentration of 5 mg L^{-1} in the presence of solid photocatalyst (0.03 g). The solution was stirred in dark for 30 min to obtain a good dispersion, reached

adsorption/desorption equilibrium between the organic MB molecule and the photocatalyst surface, and then subjected to visible light irradiation. At given irradiation time intervals, a series of reaction solutions (~3 mL) were taken out and remove the suspended catalyst particles for photocatalytic analysis. The concentration of MB was analyzed on UV-via spectrophometer 2500 by using its characteristic absorption at 660 nm. For comparison, the photocatalytic activities of commercial catalyst P25 and as-obtained TiO_2 synthesized by calcination in air were also evaluated under the same conditions.

Electrochemical evaluation The working electrode was fabricated with the as-prepared TiO_2@C or TiO_2, acetylene black (AB) and polytetrafluoroethylene (PTFE) in a weight ratio of 7 : 2 : 1. A small amount of 0.5 M H_2SO_4 solution was added to make a homogeneous mixture, which was then smeared onto the graphite substrate (1 cm^2) for subsequent electrochemical measurement by cyclic voltammetry (CV) and chronopotentiometry (CP) and electrochemical impedance spectroscopy (EIS) tests performed on an IVIUM electrochemical workstation (the Netherlands). The typical loading of the electroactive TiO_2@C or TiO_2 is 7 mg cm^{-2}. All experiments were carried out in a three-electrode cell with a working electrode, a platinum plate counter electrode (1 cm^2) and a saturated calomel electrode (SCE) reference electrode. The electrolyte was 0.5 M H_2SO_4 solution. Cycling performance was carried out with a CT2001D tester (Wuhan, China). The SCs were calculated by using the following equation:

$$SC = \frac{It}{\Delta V} \quad (1)$$

where I, t and ΔV denoted the discharge current (A g^{-1}), discharge time (s), and the discharge potential interval (V), respectively.

3. Results and discussion

3.1 Physicochemical, textural and structural characterizations

In the typical synthetic protocol, as depicted in **Fig. 1a**, we herein used the EG instead of DI water to manipulate the hydrolysis and condensation rates of the TBOT. After mixed with EG, TBOT would react with EG to form colorless solution of titanium glycolate or mixed alkoxide/glycolate derivatives, as demonstrated by the following two equations (2, 3).[20, 21]

$$Ti(OBu)_4 + HOCH_2CH_2OH \rightarrow Ti(OCH_2CH_2O)(OBu)_2 + 2HOBu \quad (2)$$

$$Ti(OBu)_4 + 2HOCH_2CH_2OH \rightarrow Ti(OCH_2CH_2O) + 4HOBu \quad (3)$$

When the colorless solution is added dorpwise into the light-yellow EG solution of Rutin (the step I in **Fig. 1a**), a scarlet solution is obtained accordingly, which should be ascribed to the strong interaction between titanium alkoxide/glycolate and Rutin. After following solvothermal treatment at 180 °C for 10 h (the step II in **Fig. 1a**), latericeous Rutin-Ti powder was obtained. **Fig. 1b** displays typical wide-angle XRD pattern of the resulting Rutin-Ti sample. Obviously, a very low and broad signal located at 2θ = 25.3 ° indicates the formation of TiO_2 nanocrystallites. However, it should be still pointed out that the existence of amorphous phase cannot be excluded under this circumstance.

To further investigate the specific composition and structure of the Rutin-Ti product, FT-IR measurements were carried out accordingly. Corresponding spectra were recorded for the Rutin-Ti and Rutin (**Fig. S1**, Electronic Supporting Information, ESI†), and specific assignments of the bands are also comparatively collected (**Table S1**, EIS†). Evidently, the FT-IR spectrum of Rutin-Ti is similar to that for Rutin just with the exception of another two bands emerging at 638 and 499 cm^{-1}, which are generally ascribed to typical Ti-O stretching bend associated with titanium glycolate/amorphous materials,[20] and the anatase TiO_2,[22] respectively. As reported

previously,[20] a little water in EG system is one key reagent for the formation of anatase nano-TiO_2. Therefore, we believe that the observation of nanophase TiO_2 here should be ascribed to the contribution from the crystal water in Rutin trihydrate over solvothermal process. After careful examination, it is inspected easily that the stretching vibrations of ν(C=O) and ν(C-O-C) both shift to lower wave number in the spectrum of Rutin-Ti, when compared to those for the Rutin (**Fig. S1** and **Table S1,** EIS†), which reveals the evident coordination between the Rutin and titanium glycolate/anastase TiO_2. It is owing to the strong interaction that a scarlet solution is unexpected obtained when the colorless EG solution of TBOT is mixed with the light yellow EG solution of Rutin, as discussed above. Also for the same reason, the titanium glycolate/anastase TiO_2 would be highly expected to be dispersed uniformly in the as-fabricated Rutin-Ti at the nanoscale. Such unique nanohybrid can efficiently restrain the growth of the formed nanosized TiO_2, and facilitate the *in-situ* coating the nano-TiO_2 core with uniform carbon shell meanwhile during the annealing in N_2 atmosphere at enhanced temperature. With further calcination in air, the carbon species is oxidized partially after the step III in **Fig. 1a**, and black core-shell TiO_2@C is obtained with a low carbon content of ~3 wt.% (**Fig. S2**, EIS†).

Fig. 1c shows the representative powder XRD pattern of as-synthesized core-shell TiO_2@C nanohybrid. Apparently, nine reflection peaks appear at 2θ = 25.3 ° (101), 48.0 ° (112), 37.8 ° (200), 53.9 ° (105), 55.0 ° (211), 62.7 ° (204), 68.8 ° (116), 70.3 ° (220) and 75.0 ° (215), respectively, which can be successfully indexed to the anatase TiO_2 with tetragonal space group I41/amd (141), compared to the standard pattern (JCPDS no. 21-1272) marked by the blue vertical lines. In general, the transition temperature of the anatase to rutile phase is at ~600 °C.[23] Interestingly, no any rutile TiO_2 is found in our study after calcinated even at 700 °C, which suggests

that the carbon species involved in the hybrid can effectively suppress the anatase-rutile transition.[24, 25] Of note, the broader diffraction peaks with lower intensity are observed for the TiO_2@C sample, suggesting the smaller size of the TiO_2 core in the hybrid, compared to the white TiO_2 (the inset in **Fig. 1c**) obtained directly by annealing in air, which strongly confirms that the existence of carbon shell can inhibit the growth and/or aggregation of the nano-scaled TiO_2 during high-temperature annealing to a certain extent.

Furthermore, it is worthy of noting that typical peaks related to the carbon phase cannot be discerned in **Fig. 1c**. To further verify the carbon species in the core-shell sample, corresponding Raman spectrum of the TiO_2@C from 1080 to 2450 cm^{-1} is demonstrated in **Fig. 1d**. Two typical vibrational modes of carbonaceous materials, that is, the D-band centered at ~1370 cm^{-1} (A_{1g}) and the G-band sitting at ~1596 cm^{-1} (E_{2g}),[26, 27] are distinctly presented. According to the intensity ratio (~1.1) of the D- to G-band and the XRD result (**Fig. 1c**) above, the amorphous form of the carbon shell in the nanohybrid is convincible here. As a consequence, the low content and amorphous nature of the carbon in the nanohybrid should be responsible well for the absence of diffraction peaks for carbon species, as seen from **Fig. 1c**.

As is established before,[4] the carbonthermal reduction commonly occurs over high-temperature carbonization in N_2 atmosphere. Raman spectroscopy in the wavenumber range of 300 – 800 cm^{-1} is next carried out to investigate the effect of carbon shell upon the Ti species in the final TiO_2@C product. As observed in **Fig. 3e**, typical bands of anatase-phase TiO_2 are both displayed clearly for the TiO_2 and TiO_2@C. In specific, the peaks at 393.5/400.1, 510.9/519.7, and 632.3/635.2 cm^{-1} should be attributed to the B_{1g}, A_{1g} or B_{1g}, and E_g modes of TiO_2 with anatase structure, respectively. Of particular note, these characteristic peaks are both blue shifted for the

TiO_2@C, when compared to those for phase-pure TiO_2, suggesting the existence of oxygen vacancies, *i.e.*, Ti^{3+} sites in the as-fabricated hybrid TiO_2@C.[4, 12, 28, 29]

More detailed information about the specific chemical and bonding environment of the resulting TiO_2@C is further ascertained by using XPS measurements, and corresponding results are summarized in **Fig. 2**. The full spectrum of the TiO_2@C is shown in **Fig. 2a**, and Ti, O and C species are all detected on the surface of the nanohybrid. By using a Gaussian fitting method, the Ti 2p emission spectrum is best fitted, and the Ti 2p high-resolution XPS spectrum is analyzed in **Fig. 2b**, characteristic of Ti^{4+} and Ti^{3+}. Specifically, the typical binding energies (BEs) of Ti^{4+} at 458.6 (Ti $2p_{3/2}$) and 464.5 (Ti $2p_{3/2}$) eV are evident obviously. Besides, another fitted peak at BE of 463.4 eV is the contribution from the Ti^{3+} species in the sample. The ratio of trivalent to tetravalent Ti is calculated to be ~3.1 : 96.9. **Fig. 2c** shows the C 1s fine XPS spectrum. Clearly, the main C 1s peak is dominated by elemental carbon at BE of 284.6 eV, attributed commonly to extensively delocalized alternant hydrocarbon. The peak at 283.8 eV can be assigned to the representative Ti-C bond.[30, 31] The shift of BE for Ti-C (~282.0 eV) to a higher energy should be reasonably related to the decreased electron density around the Ti atom in the O-Ti-C bond, compared to that in the C-Ti-C bond.[30, 32] Thus, the C doped into the TiO_2 lattice is confirmed by forming an O-Ti-C bond. Moreover, the observed peak at 285.8 eV should be ascribed to the contribution of C-O species, thus it can be inferred that a carbon atom may also occupy the site of the titanium atom, to form a Ti-O-C bond.[30, 33] As for the O spectrum (**Fig. 2d**), the peaks at BEs of 530.1 and 531.7 eV correspond to Ti-O-Ti (lattice O) and O-H[30] on the surface of the core-shell TiO_2@C, respectively.

Fig. 3 demonstrates the representative morphology of the as-obtained TiO_2@C

specimen. As seen in **Fig. 3(a**, **b)**, simple loose aggregation of nanoparticles (NPs) is explicitly evident. It is easy to note the uniform distribution of Ti, O and C elements in the resulting nanohybrid, as observed from the EDX mapping images (the inset in panel a). To reveal the specific micro-structures of the TiO_2@C more clearly, (HR)TEM measurements are carried out accordingly, and typical images are demonstrated in **Fig. 4(a-f)**. A spherical aggregation of ~400 nm in size, as displayed in **Fig. 4a**, which are constructed evidently with lots of NPs. Corresponding EDX data (**Fig. S2**, EIS†), obtained from the red rectangular region in **Fig. 4a**, suggests the co-existence of Ti, O and C elements in the hybrid TiO_2@C. Furthermore, the EDX mapping images (**Fig. 4b**) clearly reveal the uniform distribution of the three species in the as-fabricated nanohybrid at the nanoscale once more. As seen from the higher-magnification TEM image (**Fig. 4c**), detected from a sampling area indicated by the green rectangle region in **Fig. 4a**, the unique loose structure is composed of primary NPs subunits, and presents a typical wormhole meso-framework. The interlinked mesopores between the NPs would allow light scattering inside their pore channels and thus enhance the light harvesting, as reported previously,[8, 34] and also render the electrolyte rapid transportation in the hybrid meanwhile. HRTEM results are presented in **Fig. 4(d-f)**. Apparently, amorphous carbon phase is deposited either on the surface and/or between TiO_2 NPs with discernable crystalline fringes, as shown in **Fig. 4d**. TEM image of a single TiO_2@C particle is also shown in **Fig. 4e**, where a typical core-shell structure consisting of a crystalline TiO_2 core of ~13 nm in size and carbon shell with a thickness of ~1 – 3 nm is observed. Similar structure is also evident in **Fig. 4f**, which is taken from the blue rectangle region in **Fig. 4c**. The clear fringes observed in **Fig. 4(e**, **f)** correspond to the interplanar distances of ~0.19 and ~0.23 nm, respectively, which agree well with the lattice spacings of the (202) and

(112) planes for the anatase TiO_2. **Fig. 4g** demonstrates the SAED pattern with a series of concentric rings along with a spot pattern, revealing the polycrystalline characteristics of the TiO_2 core, which matches well with (101), (112), (200), (105), (204), (116) and (215) planes of the anatase TiO_2, respectively. This is in good correspondence with the XRD analysis above (**Fig. 1c**).

The mesoporosity and textural properties of the unique TiO_2@C product are further studied by N_2 adsorption-desorption measurement. Typical sorption isotherms are presented with typical IV sorption behavior, as illustrated in **Fig. 5a**, according to the IUPAC classification. A distinct hysteresis loop sitting in the larger pressure range of > 0.8 P/P_0 suggests the inherent mesoporous feature of the resulting TiO_2@C nanohybrid, which can be further verified by the pore size distribution (PSD) data in **Fig. 5b**, where the pore size is mainly ranged from 2.0 to 50 nm. The textural properties of the resultant TiO_2@C are quantitatively summarized as follows: the Brunauer-Emmett-Teller specific surface area (SSA), mesoporous volume, and average pore size are ~130 m^2 g^{-1}, ~0.43 cm^3 g^{-1}, ~12.5 nm, respectively. With the crystallite size of the TiO_2@C and corresponding TEM images (**Fig. 4(a, c)**) in mind, the mesopores are believed to be produced by the aggregation and connection of the adjacent TiO_2@C NPs with the core-shell nano-architecture.

3.2 Photocatalytic characterization

The optical absorption property, corresponding separation and migration of the light induced electrons and holes of a semiconductor photocatalyst are recognized as the vital aspects in determining its photocatalytic activity.[35, 36] Diffuse reflectance spectroscopy is often utilized to characterize the optical absorption properties of the photocatalysts, and corresponding electron states in the photocatalysts. **Fig. 6a** presents the UV-vis diffuse reflectance spectra of the as-prepared TiO_2 and TiO_2@C

samples. As expected, strong absorption property in the UV light region is observed for the TiO_2 powders. In contrast, the core-shell TiO_2@C shows an enhanced absorption capacity in the range of 200 – 800 nm. And the strong absorption region is extended to the visible region from the UV light region, owing to the synergetic effect of the carbon shell coating upon the TiO_2 core,[7-9, 16, 17] the Ti^{3+} sites,[8, 37] and the C-doping.[18, 30, 37]

Since the TiO_2@C nanohybrid possesses remarkable light absorption in visible region, we expect its appealing photochemical activity in the visible light region. Accordingly, photocatalytic activities of the TiO_2 and TiO_2@C nanohybrid are systematically evaluated by photocatalytic degradation of the MB as a test reaction under the visible light irradiation, where the commercial P25 is also applied for comparison. **Fig. 6b** collects the photocatalytic degradation rate of the dye MB over the resulting photocatalysts as a function of the irradiation time, where C is the absorption of MB at the wavelength of 664 nm after irradiation time of t, and C_0 is the absorption after the adsorption equilibrium on the samples before irradiation. For comparison, the direct photolysis test (that is, just MB without any catalyst) under the visible light irradiation, and the dark adsorption experiment in the presence of the core-shell TiO_2@C are also performed. Apparently, the visible light induced self-degradation of MB is negligible, as indicated by the photolysis behavior in **Fig. 6b**. The dark experiment with the as-prepared TiO_2@C sample demonstrate its strong adsorption capacity for MB, and the adsorption de-colorization rate of MB over the TiO_2@C is even close to ~40%, which should be reasonably attributed to its typical mesoporosity and large SSA, as mentioned above. Strikingly, assisted by the visible light irradiation, the degradation rate of MB is up to near 100% just after ~3 h of visible light irradiation, much higher than those of pure TiO_2 (11.5%) and the

commercial P25 (23.6%). Except for the adsorption removal, both of TiO_2 and P25 almost show the activity comparable with the self-degradation of MB under the same irradiation conditions, suggesting their extremely weak photocatalytic activities under the visible light irradiation, which is consistent with the report before.[7]

On the basis of experimental results above, the appreciable visible photocatalytic performance observed here for the core-shell TiO_2@C should be rationally ascribed to the following contributions, as proposed in **Fig. 7**. Firstly, the carbon incorporation into the crystalline lattice of the TiO_2 modifies the electronic band structure of TiO_2, leading to an extra C-doping level above the O2p valance band (VB), which results in the narrowing of the band gap of TiO_2 and shifts the optical absorption edge to the visible light region.[18, 30, 37-40] Secondly, the 3d orbital of the formed Ti^{3+} states (*i.e.*, oxygen vacancies) generated during carbonthermal reduction provides a donor energy below the conduction band (CB), improving the visible light response of TiO_2 itself.[8, 37] Thirdly, the surface-coating carbon species can enhance the visible light absorption and reduce the reflection of light as a photosensitizer. Moreover, the carbon shell generates electrons under visible light irradiation, thereby transferring the donated electrons to the CB of TiO_2 through Ti-O-C bonds,[41, 42] while the generated holes stay electronically and structurally near the VB of TiO_2, which can greatly enhance the transfer efficiency of photo-generated carriers. Furthermore, the low carbon content is manifested in a thin coating shell layer, enabling the MB solution to reach the active sites easier and faster. Fourthly, the dye of MB itself also partially absorbs visible light due to its photosensitization effect,[43, 44] and the photo-generated electrons are transferred to the excited state from the ground state of the dye ascribing to intramolecular π-π^* transition, then the photoelectrons of the excited state are immediately injected into the CB of TiO_2. Finally, an easier mass transport,

remarkable confinement of the target MB and enhanced light harvesting, which result from the mesoporous feature, are also beneficial to the achieved photocatalytic capacity of the core-shell nanohybrid with large SSA.[8, 30, 34, 45] Hence, the collected electrons in the CB of TiO_2 can react with O_2 (dissolved or adsorbed oxygen molecules) to produce active species such as superoxide radicals, and the photo-generated holes in the VB of TiO_2 can react with water to generate the active species such as hydroxyl radicals. The photo-generated holes and active radicals transfer easily to the nearby MB, and take part in the oxidation degradation.[46, 47] With the decomposition of the MB, the adsorption equilibrium is broken and more and more MB moves from the aqueous solution to the TiO_2@C interface and, subsequently, the dye of MB is wholly degraded to CO_2 and water through a series of reactions.

3.3 Electrochemical characterization

To further evaluate the potential application of the core-shell TiO_2@C for ECs, CV measurements were carried out between 0.0 and 1.0 V (*vs.* SCE) at various sweeping rates ranging from 2 to 100 mV s^{-1}, and corresponding curves have been shown in **Fig. 8**. Attractively, all the curves exhibit quasi-rectangular shapes, similar to that for the hydrogenated TiO_2,[12] which remains little change as the scan rate increases from 2 to 100 mV s^{-1}, suggesting good electrochemical capacitance of the core-shell TiO_2@C in 0.5 M aqueous H_2SO_4. Also, a couple of Faradaic redox peaks are evidently discernable in **Fig. 8a**, revealing the inherent pseudo-capacitive nature of the TiO_2@C electrode, which is generally ascribed to the cation intercalation and de-intercalation processes according to the following equation:[48-50]

$$(TiO_2)_{surface} + H_3O^+ + e^- \leftrightarrow (TiO_2^- H_3O^+)_{surface} \quad (4)$$

This can be visibly verified by the non-linear charge-discharge plots at a series of

mass-normalized currents, as shown in **Fig. 8b**. Furthermore, the observation of nearly symmetric potential-time plots at all current rates from 0.2 to 4.0 A g^{-1} suggests the high charge-discharge Coulombic efficiency of the TiO_2@C nanohybrid for electrochemical storage in aqueous H_2SO_4 solution. **Fig. 8c** shows the calculated SCs as a function of the applied current density. Strikingly, the unique core-shell TiO_2@C electrode exhibits remarkable SCs of ~210, ~186, ~156, ~122 and ~100 F g^{-1} at current densities of 0.2, 0.6, 1.0, 2.0 and 4.0 A g^{-1}. While the TiO_2 just delivers a SC of ~30 F g^{-1} at 0.2 A g^{-1}, and only ~6 F g^{-1} at a high current rate of 4 A g^{-1}. More attractively, the SCs estimated here are much higher than other TiO_2-based electodes, such as, Fe-doped TiO_2/C nanofibers (~137 F g^{-1}), [51] TiO_2-G-PPy (~57 – 202 F g^{-1}),[50] TiO_2@C cloth (~197 F g^{-1}),[13] TiO_2@C composites (~70 F g^{-1}),[10] Co-functionalized TiO_2 nanotubes (~124 F g^{-1}),[52] and so on. What is more, calculation of the pure EDLC by using an average value of 20 μF cm^2 [53] renders an EDLC of ~26 F g^{-1} for such core-shell TiO_2@C, which is even lower than the SC of 210 F g^{-1} at 0.2 A g^{-1}. As a result, it is inferred reasonably that the SCs calculated here should result mainly from the pseudo-capacitive contribution, and the Faradaic SC is estimated as ~184 F g^{-1}, corresponding to a area SC of ~1.42 F m^{-2}, which verifies its high electrochemical utilization. The electrochemical stability of the core-shell TiO_2@C electrode is evaluated at a current density of 1.0 A g^{-1}, as shown in **Fig. 8d**. Obviously, the SC retention of the core-shell TiO_2@C electrode gradually reduces, whereas the SC degradation is as small as ~2% over continuous 1200 cycles, suggesting its stable long-term cycling ability at large current density. The appealing electrochemical performance for the core-shell TiO_2@C should be rationally related to its large SSA, rich mesoporosity, smaller charge-transfer resistance and higher electronic conductivity originating from the carbon shell and Ti^{3+} sites, as confirmed by the EIS

data (**Fig. S4**, EIS†).

4. Conclusion

In conclusion, in the study, we purposefully designed and explored an bottom-up solvothermal strategy coupled with subsequent calcination to *in-situ* fabricate core-shell TiO_2@C nanohybrids. The plausible underlying formation mechanism of uniform core-shell nano-architecture was also tentatively proposed herein. Physicochemical, textural and structural characterizations demonstrated the unique core-shell TiO_2@C with a uniform ultrathin carbon shell of ~1 – 3 nm was endowed with rich mesoporosity and large specific surface area. Benefiting from the appealing structure and composition advantages, the resulting core-shell TiO_2@C exhibited remarkable visible light photocatalytic efficiency and stability for degradation of methylene blue under visible light irradiation, and attractive electrochemical capacitance in aqueous H_2SO_4 electrolyte when evaluated as a promising electrode for high-performance ECs. More significantly, the design and approach we devised herein will benefit future commercialization efforts of the core-shell TiO_2@C in visible light photocatalytic degradation of pollutants, next-generation ECs and even for advanced Li-ion batteries.

Acknowledgements

The authors acknowledge the financial support from National Natural Science Foundation of China (no. 51202004). Anhui Province Funds for Distinguished Young Scientists (no. 1508085J09), the Natural Science Foundation of Anhui Province (no. 1508085ME106, KJ2013A051), the Foundation for Young Talents in College of Anhui Province, and the Opening Project of CAS Key Laboratory of Materials for Energy Conversion (no. 2014001).

† Electronic Supplementary Information (ESI) available: FT-IR spectrum, TG, EDX and EIS data of the controlled experiments. See DOI: 10.1039/b000000x/

Notes and References

[1] A. Zana, C. Rüdiger, J. Kunze-Liebhäuser, G. Granozzi, N. E. A. Reeler, T. Vosch, J. J. K. Kirkensgaard and M. Arenz, *Electrochim. Acta*, 2014, **139**, 21.

[2] G. Q. Zhang, H. B. Wu, T. Song, U. Paik and X. W. Lou, *Angew. Chem. Int. Ed.*, 2014, **53**, 12590.

[3] Z. W. She, W. Li, J. J. Cha, S. S. Hong and Y. Cui, *Nat. Commun.*, 2013, **4**, 1331.

[4] J. Y. Li, B. Ding, G. Y. Xu, L. R. Hou and X. G. Zhang, *Nanoscale*, 2013, **5**, 5743.

[5] L. K. Tsui, J. Huang, M. Sabat and G. Zangari, *ACS Sustainable Chem. Eng.*, 2014, **2**, 2097.

[6] S. U. M. Khan, M. Al-Shahry and W. B. Ingler Jr, *Science*, 2002, **297**, 2243.

[7] L. Zhao, X. F. Chen, X. C. Wang, Y. J. Zhang, W. Wei, Y. H. Sun, M. Antonietti and M. M. Titirici, *Adv. Mater.*, 2010, **22**, 3317.

[8] D. H. Wang, L. Jia, X. L. Wu, L. Q. Lu and A. W. Xu, *Nanoscale*, 2012, **4**, 576.

[9] S. Shanmugam, A. Gabashvili, D. S. Jacob, J. C. Yu and A. Gedanken, *Chem. Mater.*, 2006, **18**, 2275.

[10] J. L. Liu, Z. W. Cai, Y. K. Lv, Y. J. Zhang, C. Su, M. Ouyang, C. Zhang and D. S. Wright, *J. Mater. Chem. A*, 2015, **3**, 1837.

[11] H. M. Zheng, T. Zhai, M. H. Yu, S. L. Xie, C. L. Liang, W. X. Zhao, S. C. I. Wang, Z. S. Zhang and X. H. Lu, *J. Mater. Chem. C*, 2013, **1**, 225.

[12] X. H. Lu, G. M. Wang, T. Zhai, M. H. Yu, J. Y. Gan, Y. X. Tong and Y. Li, *Nano Lett.*, 2012, **12**, 1690

[13] X. H. Lu, M. H. Yu, G. M. Wang, T. Zhai, S. L. Xie, Y. C. Ling, Y. X. Tong and Y. Li, *Adv. Mater.*, 2013, **25**, 267.

[14] Z. Zheng, J. J. Chen, R. J. Yoshida, X. Gao, K. Tarr, Y. H. Ikuhara and W. L. Zhou, *Nanotechnology*, 2014, **25**, 435406.

[15] A. Linsebigler, G. Lu and J. T. Yates, *Chem. Rev.*, 1995, **95**, 735.

[16] P. Zhang, C. L. Shao, Z. Y. Zhang, M. Y. Zhang, J. B. Mu, Z. C. Guo and Y. C. Liu, *Nanoscale*, 2011, **3**, 2943.

[17] X. Shao, W. C. Lu, R. Zhang and F. Pan, *Sci. Rep.*, 2013, **3**, 3018.

[18] R. Leary and A. Westwood, *Carbon*, 2011, **49**, 741.

[19] X. H. Lu, D. Z. Zheng, T. Zhai, Z. Q. Liu, Y. Y. Huang, S. L. Xie and Y. X. Tong, *Energy Environ. Sci.*, 2011, **4**, 2915.

[20] P. Wang, T. F. Xie, L. Peng, H. Y. Li, T. S. Wu, S. Pang and D. J. Wang, *J. Phys. Chem. C*, 2008, **112**, 6648.

[21] D. M. Puri and R. C. Mehrotra, *Indian J. Chem.*, 1967, **51**, 448.

[22] I. Ivanova, A. Harizanova and M. Surtchev, *Mater. Lett.*, 2002, **55**, 327.

[23] Y. T. Lin, C. H. Weng, Y. H. lin, C. C. Shiesh and F. Y. Chen, *Sep. Purif. Technol.*, 2013,**116**, 114.

[24] V. Loryuenyong, A. Buasri, C. Srilachai and H. Srimuang, *Mater. Lett.*, 2012, **87**, 47.

[25] M. Inagaki, *Carbon*, 2012, **50**, 3247.

[26] L. Zhou, S. Q. Zhu, H. Cao, L. R. Hou and C. Z. Yuan, *Green Chem.*, 2015, **17**, 2373.

[27] L. R. Hou, L. Lian, D. K. Li, G. Pang, J. F. Li, X. G. Zhang, S. L. Xiong and S. L. Xiong, *Carbon*, 2013, **64**, 141.

[28] X. Pan and X. Ma, *J. Solid State Chem.*, 2004, **177**, 4098.

[29] A. Golubovic, M. Scepanovic, A. Kremenovic, S. Askrabic, V. Berec, M. Z. Dohevic and Z. Popovic, *J. Sol-Gel Sci. Technol.*, 2009, **49**, 311.

[30] W. Zhou, Y. Liu, Y. Z. Zhang, G. Yang, S. H. Deng, F. Shen, H. Peng and L. L. Wang, *New J. Chem.*, 2014, **38**, 1647;

[31] L. Tian, L. Ye, K. Deng and L. Zan, *J. Solid State Chem.*, 2011, **184**, 1465.

[32] X. Wu, S. Yin, Q. Dong, C. Guo, H. Li, T. Kimura and T. Sato, *Appl. Catal. B*, 2013, **142-143**, 450.

[33] D. Wang, L. Xiao, Q. Luo, X. Li, J. An and Y. Duan, *J. Hazard. Mater.*, 2011, **192**, 150.

[34] J. H. Pan, X. W. Zhang, A. J. Du, D. D. Sun and J. O. Leckie, J. Am. Chem. Soc., 2008, 130, 11256.

[35] S. Meng, W. Z. Wang, J. Ren, S. M. Sun, L. Wang and L. Zhang, *J. Mater. Chem.*, 2009, **19**, 6213.

[36] L. Kong, Z. Jiang, T. C. Xiao, L. F. Lu and M. O. Jones, *Chem. Commun.*, 2011, **47**, 5512.

[37] Y. C. Liu, M. Y. Xing and J. L. Zhang, *Chin. J. Cataly.*, 2014, **35**, 1511.

[38] H. X. Lin, W. H. Deng, T. H. Zhou, S. B. Ning, J. L. Long and X. X. Wang, *Appl. Catal. B*, 2015, **176-177**, 36.

[39] H. Q. Zhuang, Q. Gu, J. L. Long, H. Lin, H. X. Lin and X. X. Wang, *RSC Adv.*, 2014, **4**, 34315.

[40] Z. Z. Zhang, X. X. Wang, J. L. Long, Q. Gu, Z. X. Ding and X. Z. Fu, *J. Catal.*, 2010, **276**, 201.

[41] J. Zhou, F. Chen and J. L. Zhang, *J. Phys. Chem. C*, 2010, **114**, 933.

[42] J. C. Liu, W. Y. Zhu, S. Y. Yu and X. L. Yan, *Carbon*, 2014, **79**, 369.

[43] J. W. Tang, Z. G. Zou and J. H. Ye, *Chem. Mater.*, 2004, **16**, 1644.

[44] X. T. Pian, B. Z. lin, Y. L. Chen, J. D. Kuang, K. Z. Zhang and L. M. Fu, *J. Phys. Chem. C*, 2011, **115**, 6531.

[45] F. Deng, X. Luo, K. Li, X. Tu, S. Luo, L. Yang, N. Zhou and H. Shu, *J. Mol. Catal. A: Chem.*, 2013, **366**, 222.

[46] L. M. Zhang, S. Diao, Y. F. Nie, K. Yan, N. Liu, B. Y. Dai, Q. Xie, A. Reina, J. Kong and Z. F. Liu, *J. Am. Chem. Soc.*, 2011, **133**, 2706.

[47] D. M. Chen, Z. H. Wang, T. Z. Ren, H. Ding, W. Q. Yao, R. L. Zong and Y. F. Zhu, *J. Phys. Chem. C*, 2014, **118**, 15300.

[48] Q. H. Huang, X. Y. Wang, J. Li, C. L. Dai, S. Gamboa and P. Sebastian, *J. Power Sources*, 2007, **164**, 425.

[49] T. Bordjiba and D. Bélanger, *J. Electrochem. Soc.*, 2009, **156**, A378.

[50] J. L. Jiang, X. Lu, C. M. Xie, G. J. Wan, H. P. Zhang and Y. H. Tang, *J. Phys. Chem. C*, 2015, **119**, 3903.

[51] G. M. K. Tolba, M. Motlak, A. M. Bastaweesy, E. A. Ashour, W. Abdelmoez, M. El-newehy and N. A. M. Barakat, *Int. J. Electrochem. Sci.*, 2015, **10**, 3117.

[52] L. R. Hou, C. Z. Yuan, D. K. Li, L. F. Shen and X. G. Zhang, Mater. Lett., 2011, 65, 2632.

[53] C. Z. Yuan, J. Y. Li, L. R. Hou, J. D. Lin, X. G. Zhang and S. L. Xiong, *J. Mater. Chem. A*, 2013, **1**, 11145.

Figures and Captions

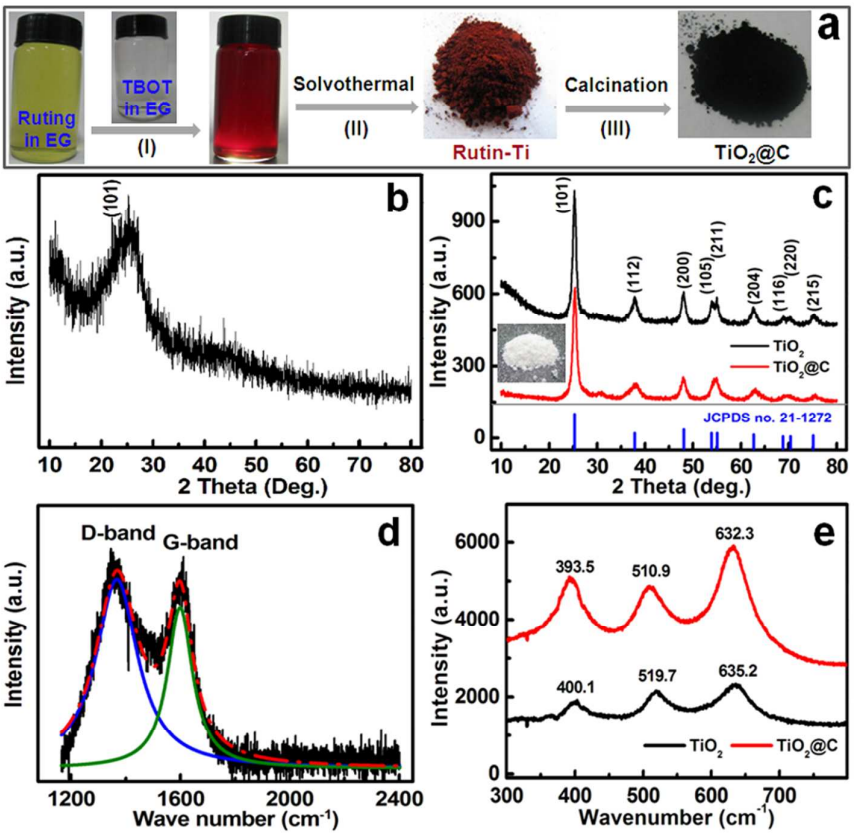

Fig. 1 Schematic illustration for synthetic process of the core-shell TiO_2@C (a); wide-angle powder XRD patterns of the Rutin-Ti (b) and the resulting TiO_2 and TiO_2@C (c); Raman spectra of the TiO_2@C (d, e) and TiO_2 (e)

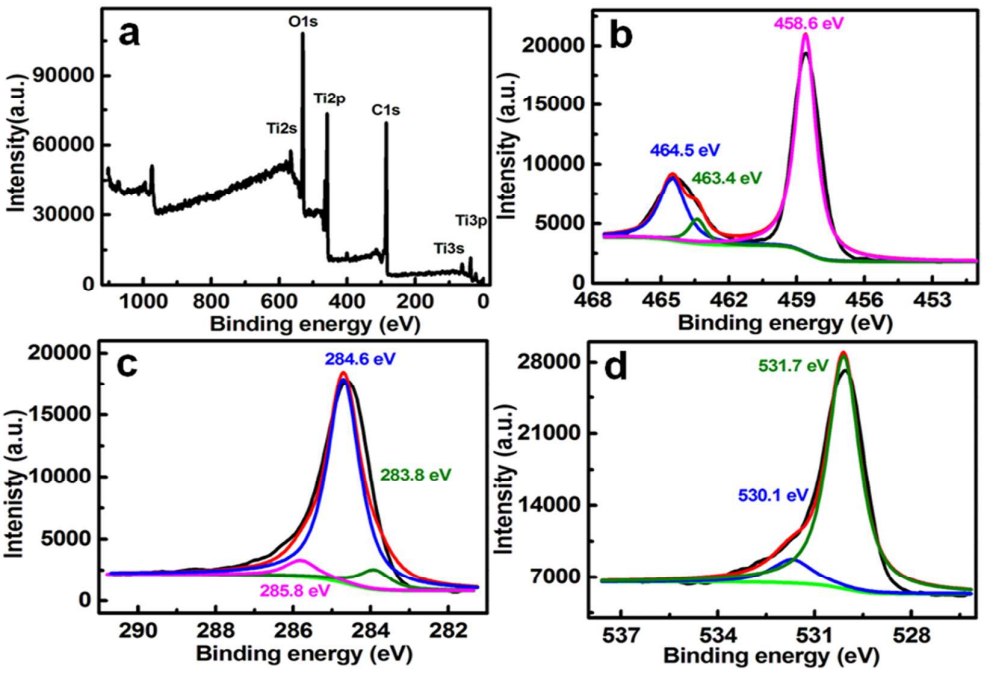

Fig. 2. Full survey spectrum (a), high-resolution Ti 2p (b), C 1s (c) and O 1s (d) XPS spectra for the core-shell TiO_2@C nanohybrid

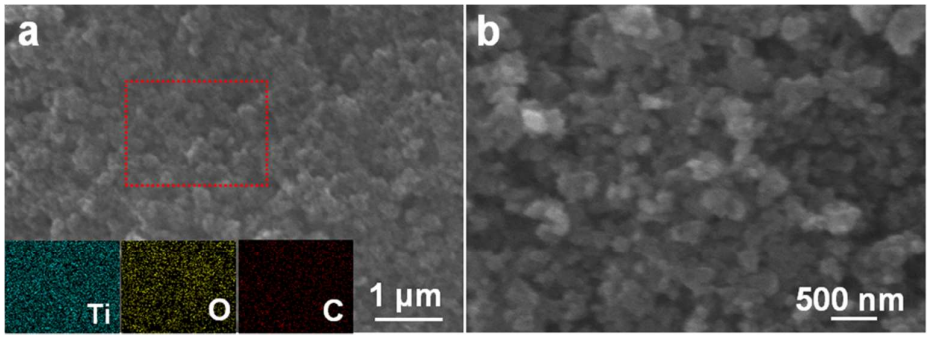

Fig. 3 FESEM images (a, b) and the corresponding EDX mapping (the inset in penal a) of the Ti, O, and C phases for the TiO_2@C. The image in (b) taken from the red rectangle region in the panel (a)

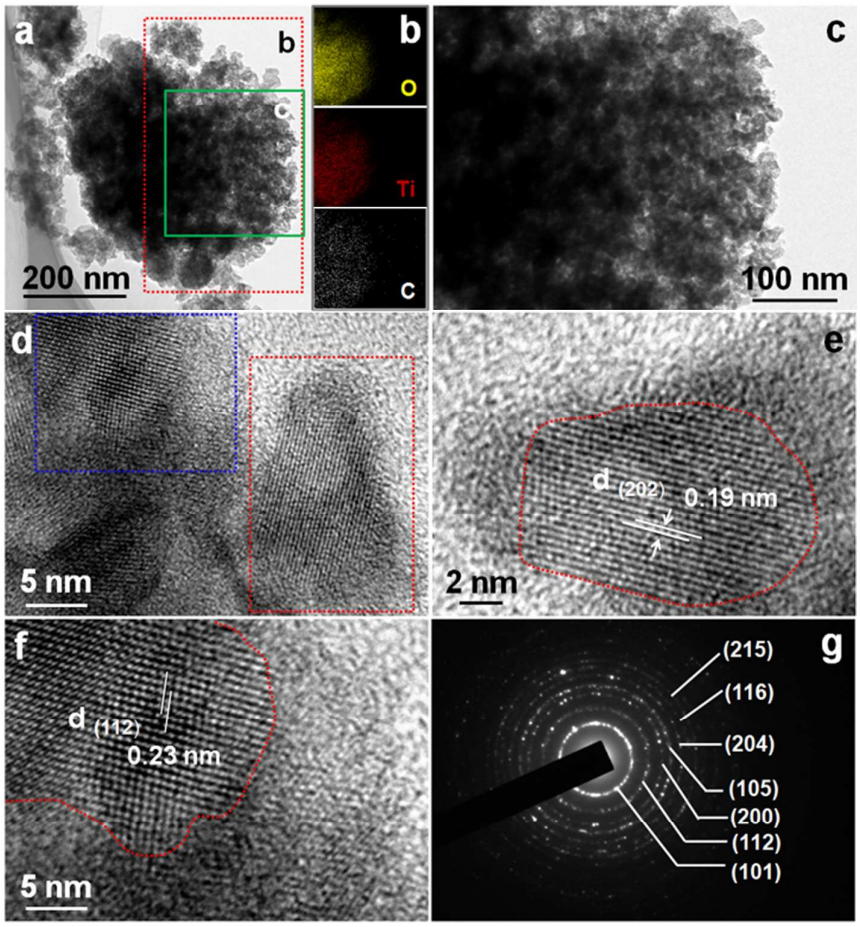

Fig. 4 TEM images (a, c), elemental mapping images (b) taken from the red rectangle region in the panel (a), HRTEM images (d-f), and SAED pattern (g) of the TiO_2@C nanohybrid. The image in (b) is taken from the green rectangle region in panel (a). The images in (e) and (f) are the magnified ones of the red and blue rectangle regions in panel (d), respectively

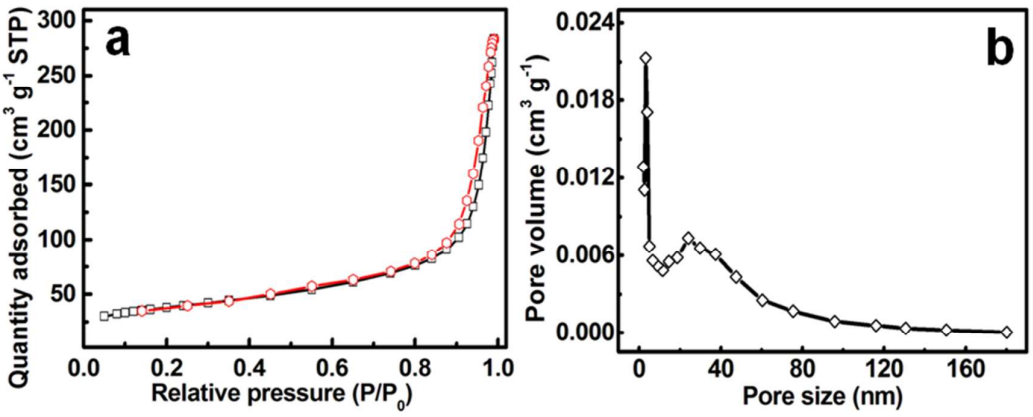

Fig. 5 N_2 adsorption isotherms (a) and PSD (b) of the core-shell TiO_2@C nanohybrid

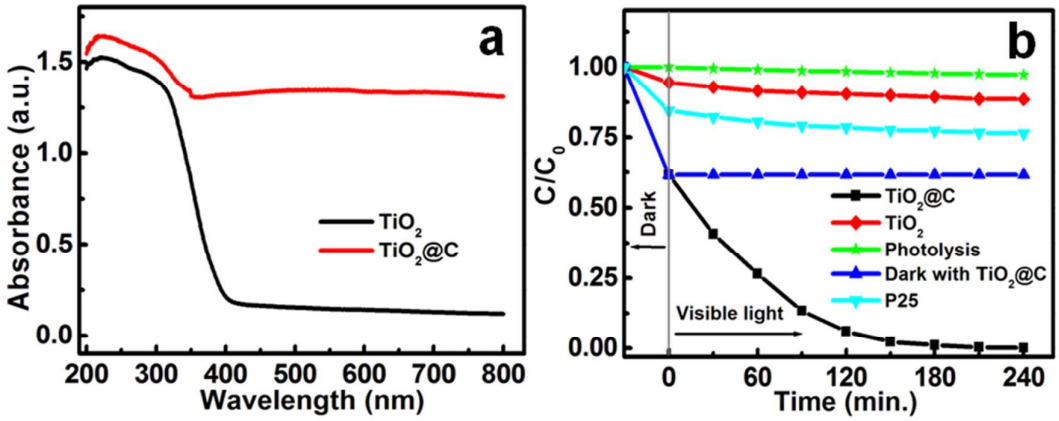

Fig. 6 UV-vis adsorption spectra (a) of the resultant TiO_2@C and TiO_2; Photocatalytic degradation profiles (b) of MB over different photocatalysts under visible light irradiation as indicated

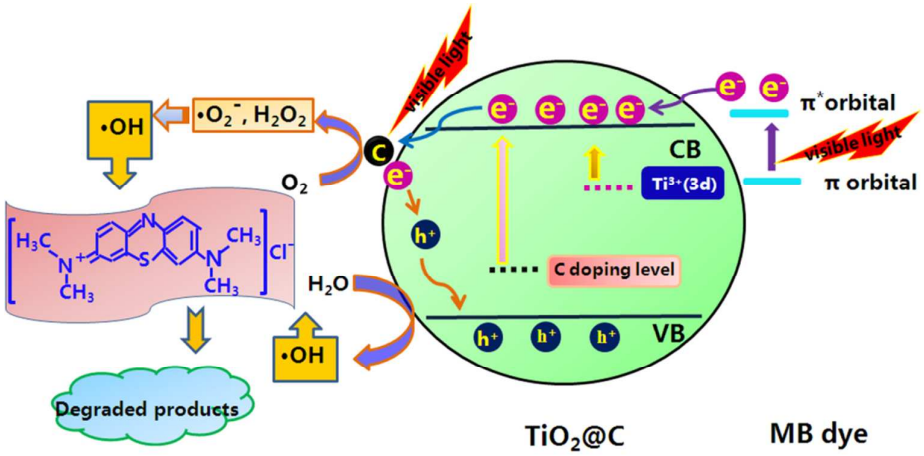

Fig. 7 Schematic illustration of electron transition and photocatalytic process of the core-shell TiO_2@C

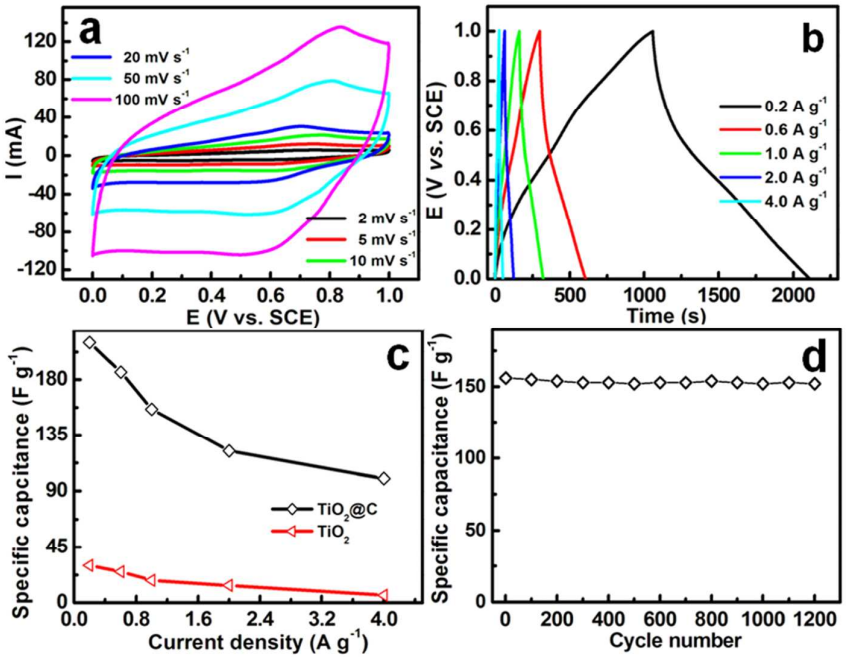

Fig. 8 Electrochemical performance: CV curves with various scan rates (a), CP plots (b), SC vs. current density (c) and cycling behavior for the core-shell TiO_2@C